Submitted Paper

Applied Spectroscopy

www.s-a-s.org

Standoff Interaction Assessment Using High-Energy Laser–Induced Oxidation Spectroscopy

Applied Spectroscopy
2023, Vol. 77(1) 17–26

DOI: 10.1177/00037028221124907
journals.sagepub.com/home/asp
SAGE

Jean-François Daigle[1], Mathieu Foster[2], Guillaume Caron[2], Adrien Amyotte[2], Dominik Pudo[1] and Francis Théberge[1]

Abstract

In light of the widespread use of high-energy lasers (HELs) for a variety of purposes, for example, standoff (>100 m) applications, will require the ability to monitor in real time the interaction with processed materials. While multiple sensing methods have been successfully developed for industrial HEL systems operating at close range, they are not compatible with the unique requirements of long-distance applications. Here, high-energy laser–induced oxidation spectroscopy (HELIOS) is demonstrated on carbon steel coupons as an efficient standoff assessment method compatible with long distance HEL applications. Acute monitoring of spectral features from thermally excited iron atoms and oxides, corroborated with real-time temperature measurements, reveals the interaction mechanisms at play.

Keywords

High-energy laser-induced oxidation spectroscopy, laser–matter interaction, spectroscopy, thermal effects, remote sensing, directed energy

Date received: 20 May 2022; accepted: 8 August 2022

Introduction

Lasers capable of producing kilowatts of continuous radiative power have already demonstrated their usefulness for a variety of industrial applications.[1] Focused on distances not exceeding a meter, these beams of light can surgically cut[2], weld,[3,4] and temper[5] thick metallic pieces, facilitating high efficiency manufacturing processes at low cost per intervention. As the technology evolved, it was rapidly discovered that a variety of parameters, including the incident laser intensity distribution, influenced significantly the interaction mechanisms, and hence the quality of end-products,[6] stimulating research for methods capable of real-time quality monitoring.[7–10] In particular, laser-based spectroscopic sensors have recently proliferated, including for improving industrial processes.[11,12] This renewed fame is attributed, in part, to all the research surrounding the integration of the SuperCam[13] on the *Perseverance* rover.

In parallel, a number of non-traditional applications have emerged, requiring operation of a high-energy laser (HEL) at distances exceeding tens of meters; sometimes even bringing the laser system outdoors and exposing the laser beam to atmospheric variations.[14] Among other applications, HEL systems have made their way in explosive ordnance disposal,[15] as well as geological exploration and mining.[16] As the distance is increased, the predictability and repeatability of the interaction no longer holds due to a variety of factors including variations of the atmospheric characteristics.

The need for novel techniques that empower real-time monitoring of laser–matter interactions stem from these uncertainties, bearing on the system's effectiveness and resulting in lower productivity. While a variety of visual, acoustic, thermal, and spectroscopic sensing methods[17] have been successfully developed to enhance the performance of industrial HEL systems, they are not compatible with the unique requirements of long-distance applications. The latter involves larger beam diameters imposed by optical diffraction as well as the absence of a pressurized gas stream evacuating the melt-pool and inhibiting oxidation. Consequently, the

[1]Valcartier Research Centre, Defence Research and Development Canada, Valcartier, QC, Canada
[2]NOVIKA Solutions, La Pocatière, QC, Canada

Corresponding author:
Jean-François Daigle, Defence Research and Development Canada, 2479 route de la bravoure, Valcartier, QC G3J1X5, Canada.
Email: jean-francois.daigle@drdc-rddc.gc.ca

resulting interaction mechanisms diverge significantly from what is generally observed at close range such that new sensors, or adaptations of existing ones, need to be developed.

High-energy laser–induced oxidation spectroscopy (HELIOS)[18] was demonstrated as an efficient technique to interrogate metallic coupons located 200 m from a multi-kW laser system, enabling standoff identification and discrimination in broad daylight. Successful attempts from an independent team have later used the approach to monitor the interaction mechanisms from a 20 m distance.[19] The technique leverages on surface oxidation accelerated by the laser–induced temperature elevation, producing distinct signatures of metallic oxides.[20]

One example is the case of carbon steel which is mainly composed of a mixture of iron (Fe) and carbon (C). Fe oxidizes rapidly when immersed in an oxygen-filled environment such as the atmosphere, more so when heated to high temperatures. As Fe(I) is the major constituent of carbon steel and the yield of C oxidation is much weaker than that of Fe, only emissions from the transitional system $D^5\Delta^4 \rightarrow X^5\Delta^4$ of iron oxide's (FeO) famous orange system have been observed.[21] In addition to the intense FeO bands, the strongest Fe(I) and Mn(I) features have been identified. Manganese is normally added to carbon steel to improve the workability and resistance to wear.

Here, HELIOS was used in a laboratory setting to demonstrate the correlation between spectroscopic signatures and the interaction phenomenology from a shorter distance. The possibility of standoff monitoring already demonstrated from a 200 m distance,[18] the laboratory configuration alleviates from the variability of atmospheric effects occurring on the outdoor range. Carbon steel coupons were exposed to HEL radiation following a systematic matrix of parameters, adjusted to fit with conditions realistically observed at a long range by varying the incident beam diameter and peak irradiance. Analysis of the gathered database revealed that significant interaction events such as the formation of a melt-pool, surface oxidation, and material vaporization are always accompanied with distinctive spectroscopic attributes, enabling real-time assessment of the reaction, and ultimately optimizing standoff interaction processes.

Expanding on what was already developed, a new feature enabling real-time temperature measurement at the interaction zone was implemented and demonstrated, providing additional information on the interaction site.

Experimental

Materials and Methods

As shown in Fig. 1 presenting the experimental configuration, testing was conducted using a commercial near-infrared laser system capable of a maximum of 15 kW (IPG, model YLS-15000). A 400 μm diameter optical fiber transported the laser energy to a reflective laser head (Kugler, model LK390). The laser head, manipulated with a robotic arm, was aligned along the horizontal plane and aimed at vertically standing SAE 1060 carbon steel coupons with 1.3 cm thickness and 10 cm sides. This configuration differs from what is observed during industrial processes where samples are usually lying flat and exposed by a laser beam propagating along the vertical direction, changing the effect of the gravitational pull on melted metal evacuation.

The composition of the SAE 1060 carbon steel samples used was 98.5% iron, 0.6% carbon, and 0.75% manganese. While its melting temperature is known at 1510 °C, the precise vaporization temperature is unknown. As the samples were mainly constituted of iron, the element's vaporization temperature of 2870 °C is assumed. Iron oxide will form at the interaction zone, catalyzed by the high temperatures induced by the laser. Similar to SAE 1060, iron oxide will melt at 1570 °C but its vaporization temperature is closer to 3400 °C.

A systematic test matrix that varied the incident beam $1/e^2$ diameters from 0.5 to 4 cm by changing the distance between the sample and the laser head was developed. For each beam diameter, the laser power was precisely adjusted such that the peak irradiance at the surface varied from 0.5 kW/cm^2 to 20 kW/cm^2. The test matrix ensured large variations in the phenomenology including thermal effects, oxidation, melt-pool formation, and material evaporation.

Three distinct sensors, each serving a specific purpose, monitored the events:

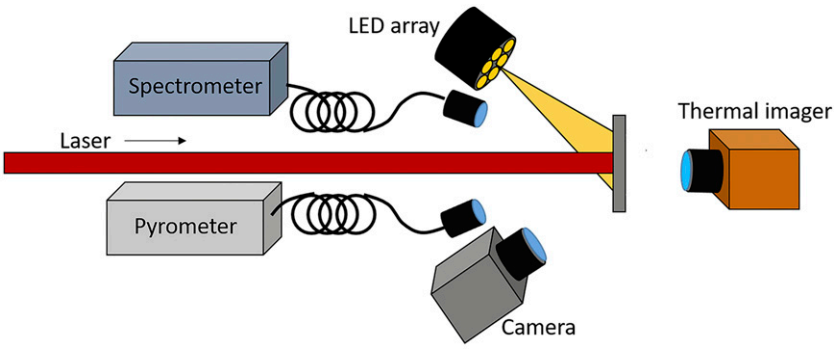

Figure 1. Experimental configuration.

(i) Phenomenology: An active imager consisting of a high-speed camera (Canadian Photonic Lab, model MS55K) and a high power, narrow band LED array (λ = 635 nm) was used to reveal the dynamics at the interaction zone. The camera sported a 50 nm wide transmission filter, matching the spectrum of the LED array that improved image contrast by minimizing the impact of the ablation plume and thermal radiation (blackbody).

(ii) Metrology: A Fluke TI300 imager was placed behind the samples, recording the thermal distribution of the back surface. The temperature measurements were used to gauge the performance of the reaction, aiming for rapid elevation. In addition, a bichromatic pyrometer IGAR12-LO aimed at the interaction site records the temporal profile of the temperature. The instrument features a dynamic range spanning from 500 °C to 2200 °C.

(iii) Reaction assessment: A grating-based spectrometer (Avaspec 3468) observed the laser-induced emissions resulting from the interaction of the laser beam with the surface. It is capable of providing temporally resolved spectra between 430 nm and 660 nm (visible) with a resolution smaller than 0.13 nm. The spectral response of the detector was calibrated, for wavelength and intensity, using a calibrated halogen light source (AvaLight-DHc).

Figure 2a presents a typical spectroscopic signature obtained in conditions of strong material vaporization when the sample was exposed to a laser beam characterized with peak intensity of 15 kW/cm^2 and 1 cm diameter. In addition to the characteristic blackbody emissions shaping the signal's background, the spectrum presents rich features including fluorescence lines from excited iron (multiple lines), manganese (403.1 nm, not shown in Fig. 2), calcium (422.7 nm), and sodium (589.0 nm, 589.6 nm) atoms as well as iron and calcium oxides. Both calcium and sodium are elements with high fluorescence yield such that even though they are not listed constituents of SAE 1060, traces or contamination can be detected. The produced emissions can be exploited to assess on the phenomenology by providing information on the thermal load accumulated on the surface, the rate of metallic oxidation and the rate of evaporation.

Figures. 2b and 2c present, respectively, a close-up of the atomic (Fe(I), 438.4 nm) and oxide (FeO, 558.9 nm) fluorescence transitions used for the analysis. For each test, the temporal evolution of the signals' amplitude was monitored by subtracting the background (dashed: long lines) from the peak signals (dashed: short lines). Additionally, the strength of blackbody emission was evaluated with the amplitude of the signal around 556.6 nm, indicated by the long, dashed line in Fig. 2c, located between two major FeO bands.[21] In order to avoid the impacts of sensor noise variations, the blackbody signal was averaged over the 30 pixels located between 555 nm and 557 nm.

Real-time temperature measurements were obtained by fitting Planck's distribution for blackbody radiation under the spectra obtained during the measurement. Using this formalism, the spectral distribution of a blackbody with temperature T is defined as:

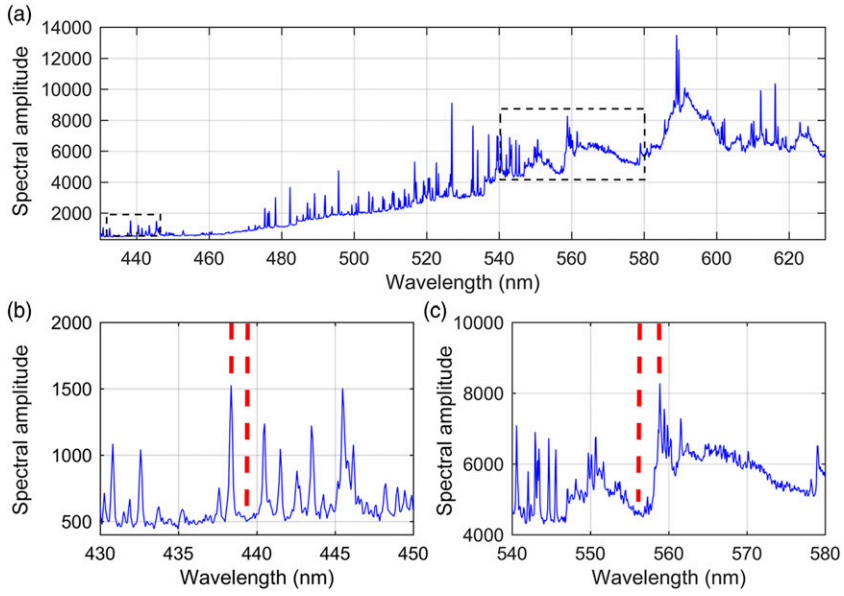

Figure 2. (a) Typical spectrum collected when the laser-induced strong metallic vaporization. Close-up of (b) Fe(I) (438.4 nm) and (c) FeO (558.9 nm) spectral features used for the evaluation. The vertical dashed lines in (b) and (c) indicate positions of peak (short lines) signal and background (long lines).

$$B(\lambda, T) = \frac{2hc^2}{\lambda^5} \frac{1}{e^{hc/\lambda k B^T} - 1} \quad (1)$$

where B is the spectral radiance distribution of an object, k_B is Boltzmann constant, h is the Planck constant, c is the speed of light, λ is the wavelength, and T is the temperature in Kelvin. As the spectrometer operates in the visible part of the spectrum, temperature measurements are only valid for surface temperatures exceeding 1700 °C. This is attributed to the weak visible signals observed at lower temperatures. It would be possible to extent the temperature measurement to lower ranges with the addition of another spectrometer monitoring in the shortwave infrared. The spectroscopic method has been used recently to measure the temperature of camera sensors during interaction with a focused laser.[22]

Results

Correlation of the spectral information obtained from the spectra with the interaction phenomenology is detailed using the three test cases presented below. Figure 3 presents a typical case describing the formation of a thin melt-pool at the surface created when a laser beam characterized by a peak intensity of 0.5 kW/cm^2 and a diameter of 4.0 cm was incident on the sample. While Figs. 3a–3c present pictures captured by the active imager highlighting the evolution of the melt-pool,

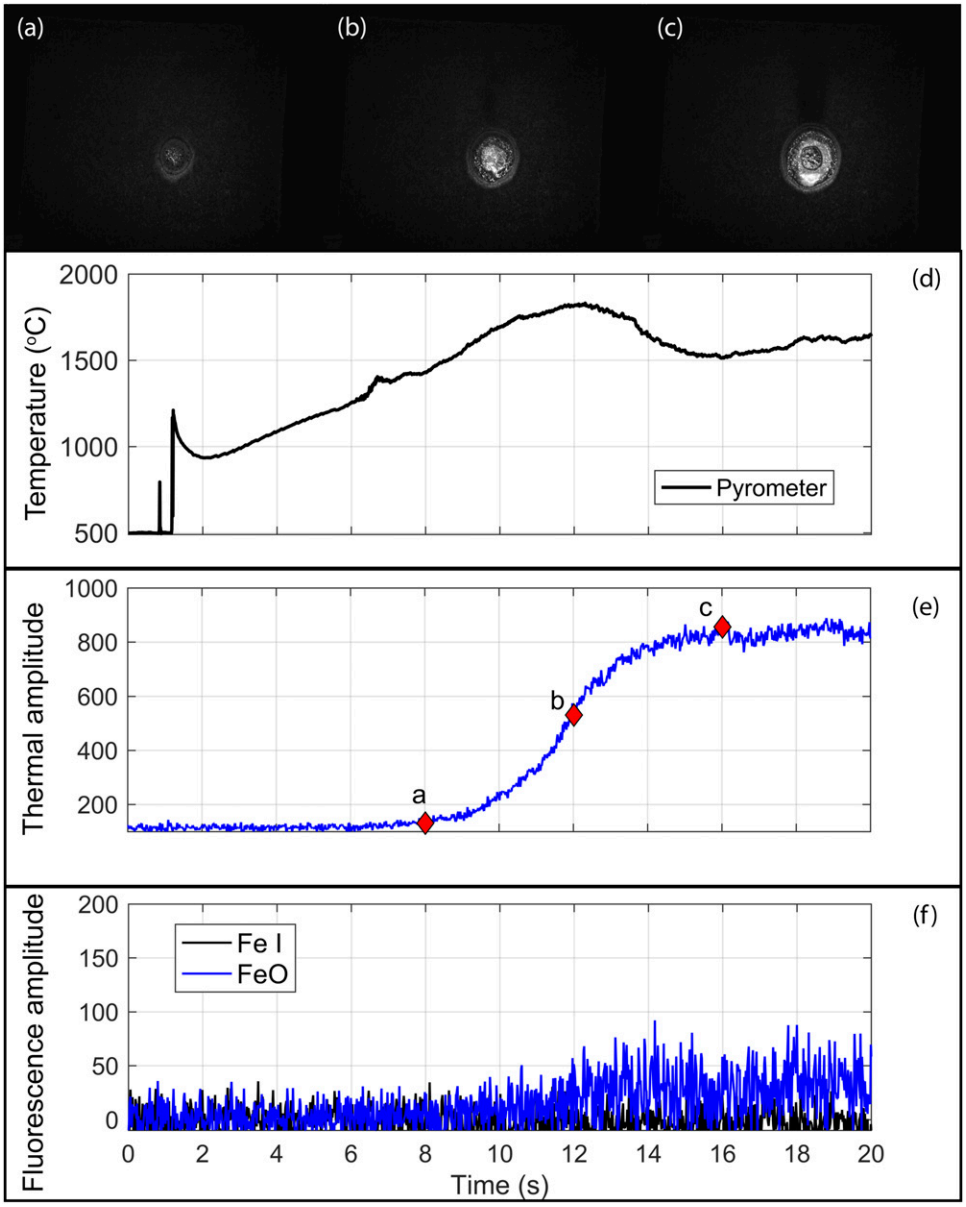

Figure 3. Results highlighting the formation of a surface melt-pool. (a–c) Selected imagery of the interaction, capture events indicated as red diamonds in (e) (d–f) Corresponding plots for the temperature, thermal, and fluorescence signals, respectively.

the temporal evolution of the surface temperature, thermal and fluorescence signals are plotted in Figs. 3d–3f, respectively. The three red diamonds in Fig. 3e indicate the moments the pictures were captured. The results indicate that the formation of the melt-pool is associated with a significant increase in thermal emission while atomic and oxides fluorescence are minimum. The thermal signal increase coincides with the surface temperature measurement by the pyrometer exceeding 1500 °C, the material's melting temperature. Consequently, a drastic rise in the thermal signal in the visible part of the spectrum is a solid indicator for the presence of liquid steel. The amplitude of the thermal signal can in fact be correlated to the volume of the active melt-pool. It is only when the surface layer reached the melting temperature that minor FeO emissions were detected. In this case, FeO emissions were 10 to 20 times weaker than for the following examples (Figs. 4 and 5) where higher laser intensities were tested. Temperature measurements using the spectroscopic method are not shown in the Fig. 3d due to the weak thermal signal produced in the visible at lower temperatures.

Similarly, Fig. 4 presents a typical situation where the laser beam was sufficiently intense to create large volumes of

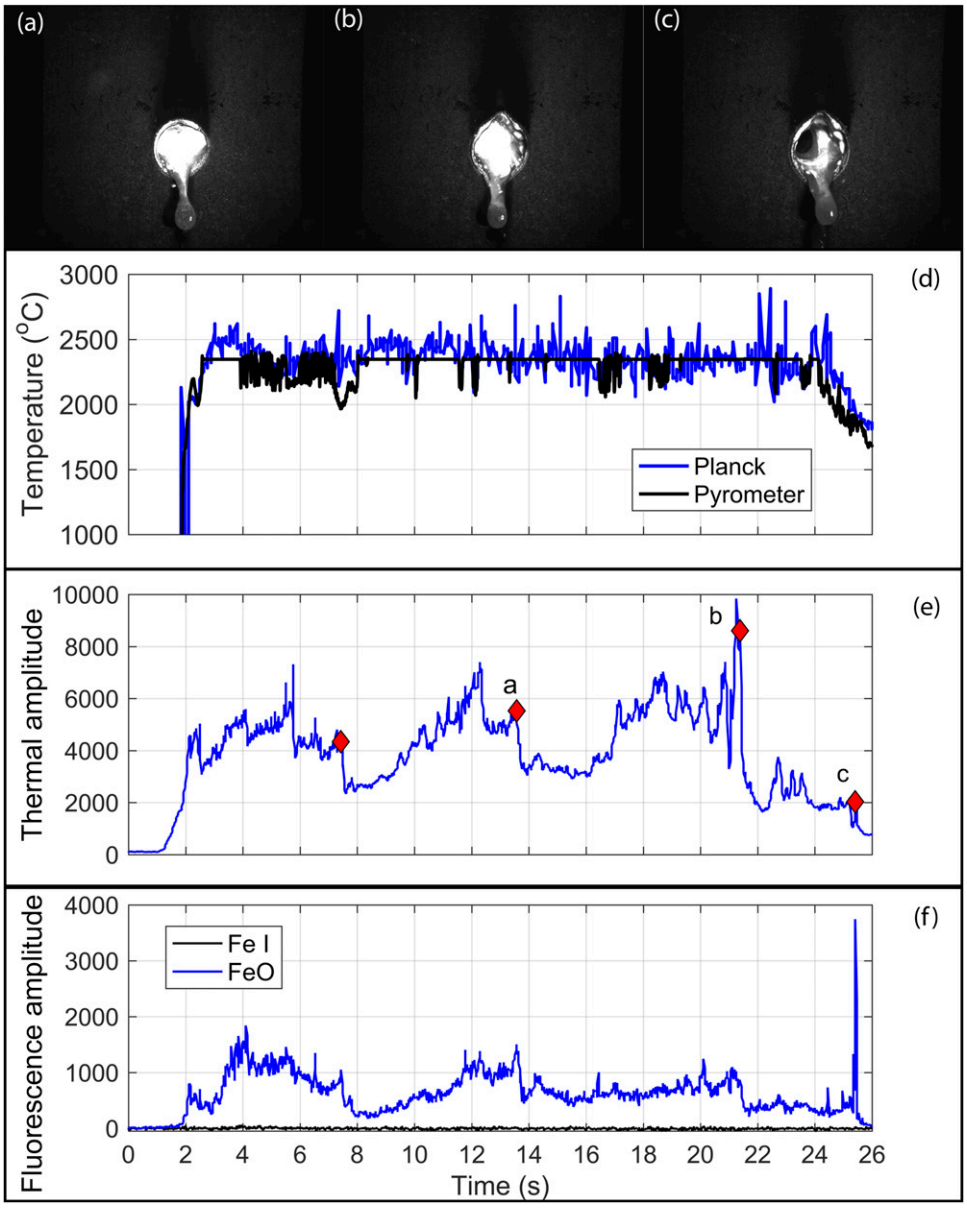

Figure 4. Results highlighting the formation of liquefied metal droplets. (a–c) Selected imagery of the interaction, capture events indicated as red diamonds in (e) Figure (d) presents the measured and calculated temperatures at the front surface of the steel plate. (e) and (f) Corresponding plots for the thermal and fluorescence signals, respectively.

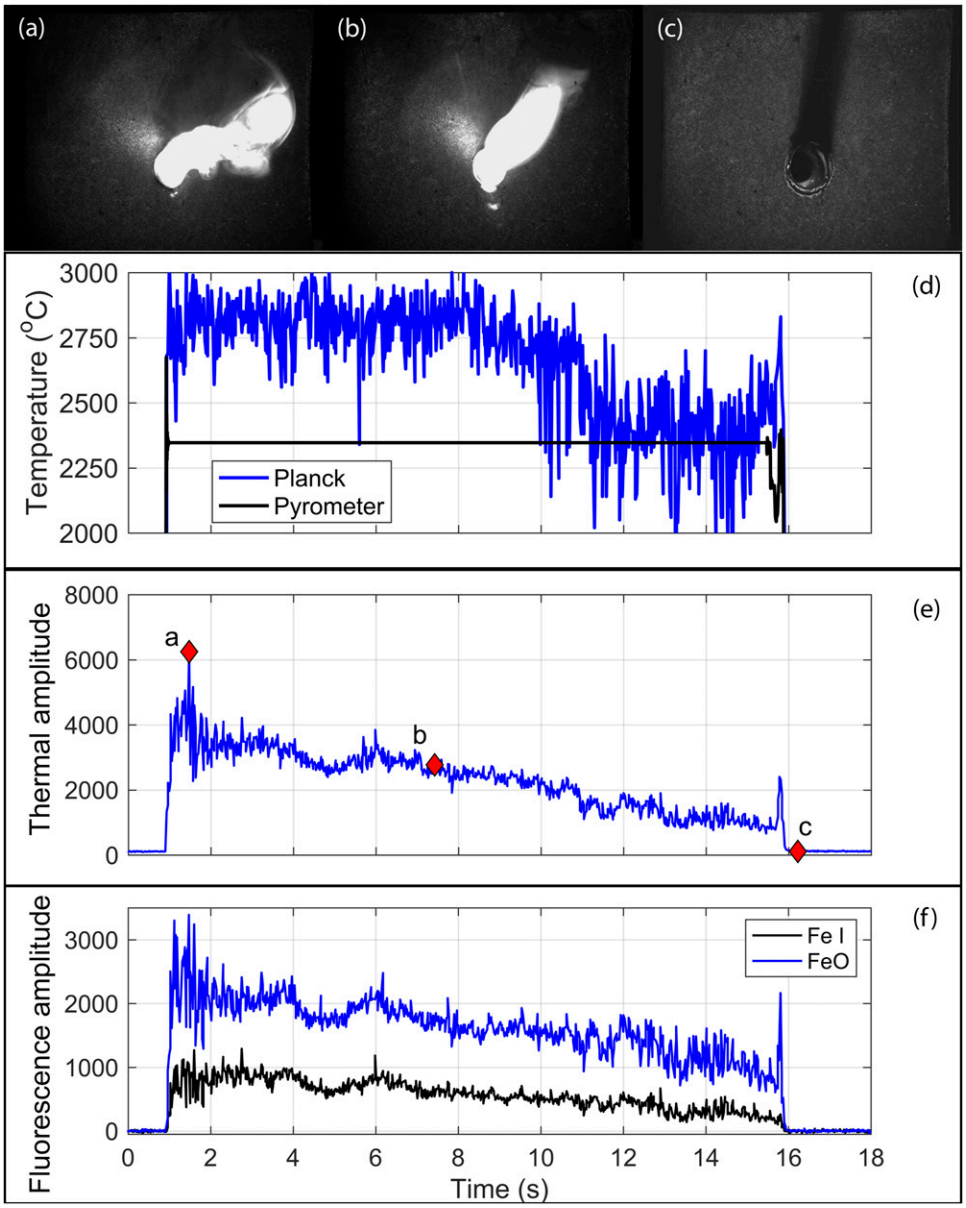

Figure 5. Results highlighting material ablation via direct vaporization (a–c) present selected imagery of the interaction, capture events indicated as red diamonds in (d) Insets (d) and (e) present the corresponding plots for the thermal and fluorescence signals, respectively.

liquefied metal periodically evacuated, under the effect of gravity, via the formation of droplets. A laser beam characterized by a peak intensity of 2.0 kW/cm^2 and a diameter of 2.0 cm was incident on the sample. The surface temperature, presented in Fig. 4d, increased rapidly above the melting point (1510 °C) and remained below the 2870 °C threshold for vaporization of iron throughout exposure. As indicated by the black curve, the surface temperature remained on the verge of the pyrometer's saturation threshold, limiting the ability of precise characterization. This is where the method using Planck's radiation distribution comes to value, extending the range of measurements. While the assessment of the method's accuracy is challenging due to the saturation of the pyrometer, the temperature range of both sensors overlapped at the beginning (2 s < time < 2.5 s) and at the end (24 s < time < 26 s) of exposure. Within these time intervals, the instruments provided similar readings.

The interaction followed a cycle where the laser beam gradually heated the sample until the volume of melted metal was sufficiently large to form a droplet. Figures 4a–4c were captured at the exact moment a droplet was evacuated. The events are indicated as red diamonds in Fig. 4e, with the last

diamond corresponding to the moment the sample was perforated. Another droplet, observed at 7.5 s, is indicated by the unlabeled diamond shown in Fig. 4e.

As seen in Fig. 4e, the cycle always started with a significant increase in thermal radiation, indicating a volume increase of the melt-pool, that persisted until the liquefied metal was removed from the interaction zone. As the droplet left the interaction zone with the thermal load it had accumulated, its removal always coincided with a significant drop in the thermal signal. Even though Fe(I) lines were absent, significant FeO emissions were detected, suggesting sustained formation of metallic oxides at the interface in contact with oxygen. While perceptible in Fig. 4e, the fluctuations associated with the evacuation of liquefied droplets are not as clear as in Fig. 4f. The large FeO peak detected at $t \approx 25$ s, which coincides with the perforation, is attributed to the interaction of the oxide layer accumulated on the sample's back surface with the laser. The oxide layer on the back surface developed during the interaction, catalyzed by the gradual thermal load deposited in the bulk by the laser beam.

Finally, Fig. 5 corresponds to a typical case where a laser beam characterized by a peak intensity of 15 kW/cm^2 and a diameter of 1.0 cm perforated the sample via material evaporation, as suggested by the brilliant plume observed in Figs. 5a and 5b. The absence of solidified droplets in Fig. 5c is also an indicator that that the transition from liquid to metal was very abrupt, the liquid material build-up being insufficient to produce the critical mass required for droplets to develop. The bright ablation plume observed in Figs. 5a and 5b is the result of the high-pressure metallic vapors formed under the influence of the laser beam. The rapid transition to the gas phase is further highlighted by Fig. 5d where temperature measurements using the spectrometer (Planck) plateaued at approximately 2870 °C, iron's vaporization temperature. The fact that it was possible to retrieve the vaporization temperature from the spectrometer reading further demonstrates the reliability of the technique. With the temperatures exceeding the pyrometer temperature range, the saturated detector failed to provide valuable information.

As opposed to the other test cases discussed previously, strong Fe(I) and FeO fluorescence signals were detected throughout the duration of laser illumination. Once again, FeO emissions spiked upon perforation of the coupon due to the oxidized layer on the back surface. A significant correlation between the signals' amplitude and the strength of the ablation plume suggests that both FeO and Fe(I) fluorescence can be used as a gauge for material vaporization, the latter being the most accurate. Indeed, while FeO can also be observed with material liquefaction, Fe(I) was only detected during aggressive evaporation regimes.

The three test cases described here demonstrated that spectroscopic analysis of the emissions resulting from the interaction of a HEL beam with matter can be used to assess the interaction phenomenology. Melt-pool formation, evacuation of metallic droplets, and material ablation at vaporization temperature were all accompanied by distinctive signatures. In addition, spectral analysis even allows quantitative temperature measurement of the exposed surface further expanding the opportunities for standoff assessment.[18]

Discussion

The predictability and repeatability of HEL interventions become challenging as the distance to the sample is increased; hence, the need for the development of sensing methods compatible with such operation regimes. Whether for pure awareness or for the purpose of closed-loop optimization, HELIOS can be used to assess the performance of a laser intervention. Optimum interaction parameters are highly dependent on the nature of the application such that there is no single definition of the performance. For the purpose of this discussion, performance was evaluated with the thermal imager (Fig. 1), measuring the time required for the sample's back surface temperature to exceed 660 °C. The apparently arbitrary threshold was selected simply because it corresponds to the thermal imager's saturation temperature. Optimal heat transfer from the laser to an object can be of interest, in particular for military applications where time of engagement may be limited.

Figure 6 presents a summary of the results obtained from the various laser intensities tested (0.5–20 kW/cm^2) and for different beam diameters (0.5–4 cm). These results shown in Fig. 6a present the average temperature of the surface measured using the spectrometer and in Fig. 6b, the average strength of the fluorescence signals for FeO and Fe(I), against the performance metric (time for the back surface to reach 660 °C). The data points in Fig. 6b were normalized with respect to the maximum signal detected to facilitate comparison. Only tests where the desired temperature was

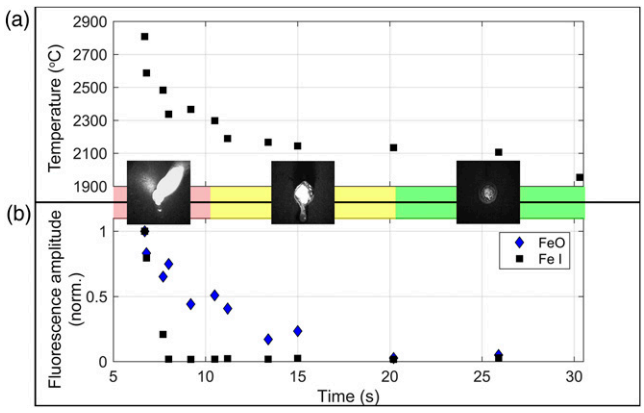

Figure 6. Each data point corresponds to the (a) surface temperature and (b) the normalized amplitude of fluorescence emissions averaged over the entire laser exposure. The results are plotted as a function of the time for reaching a back surface temperature of 660 °C.

achieved within 35 s are presented. Following the examples described above, the graph was separated in three regions highlighting the different interaction regimes observed: (i) Surface liquefaction (green), (ii) melt-pool and droplets (yellow), and (iii) evaporation (red).

The boundaries between the different interaction regimes are however very fluid and it is challenging to define clear transitions.

Based on the plots in Fig. 6, shorter dwell times are achieved when the laser beam is sufficiently intense to sustain evaporation of the material. This is highlighted by the average temperatures exceeding 2500 °C measured when the dwelling time was minimum. The shortest exposure time obtained within the test matrix exhibited a surface average temperature neighboring 2800 °C, slightly below the material's evaporation point. This is a clear indicator of the laser drilling through the sample via evaporation, the radiant plume shown in Fig. 5 is the result of the combustion of the metallic gases created. The intermediate regime, characterized with the formation of the melt-pool, resulted in longer exposure times and an increased variability in the performance metric.

As shown in Fig. 6b, laser conditions that efficiently increased the back surface temperature were all accompanied by significant FeO emissions, the average signal increasing with interaction performance. Additionally, oxidation is a highly exothermic process and produces a significant amount of heat that can be absorbed by the sample, thus accelerating the temperature elevation. Laser oxygen cutting is based on this principle.[23]

From Fig. 6b, the presence of Fe(I) emissions appears to be the dominant indicator for an efficient interaction, occurring only for the shortest exposure times when ablation is dominated by vaporization. As described earlier, Fe(I) is only observed during evaporation, when a melt-pool does not accumulate at the interaction site. In that case, heat transfer is facilitated by the gradual metallic evaporation that reduced the thickness of the sample, effectively bringing the heat front closer to the back end.

Spectroscopic assessments were also attempted on aluminum 6061 samples with identical dimensions. Figure 7a presents a typical spectrum obtained when the laser conditions were adequate for evaporation, that is, for similar phenomenology than those presented in Fig. 5. The laser beam is adjusted with a peak intensity of 20 kW/cm^2 and a diameter of 0.5 cm. The coupon was exposed for 120 s and exposure was interrupted before coupon perforation. Rich aluminum oxide features are observed between 450 nm and 550 nm, the spectrometer's resolution even resolving vibrational levels appearing as the narrow spikes sitting atop of rotational bands. Other features are attributed to magnesium oxides and smaller Al(I) emission lines.

A segment of the temperature temporal profile obtained with the spectral analysis method described above is presented in Fig. 7b. The plot concentrates on the 40 s of the

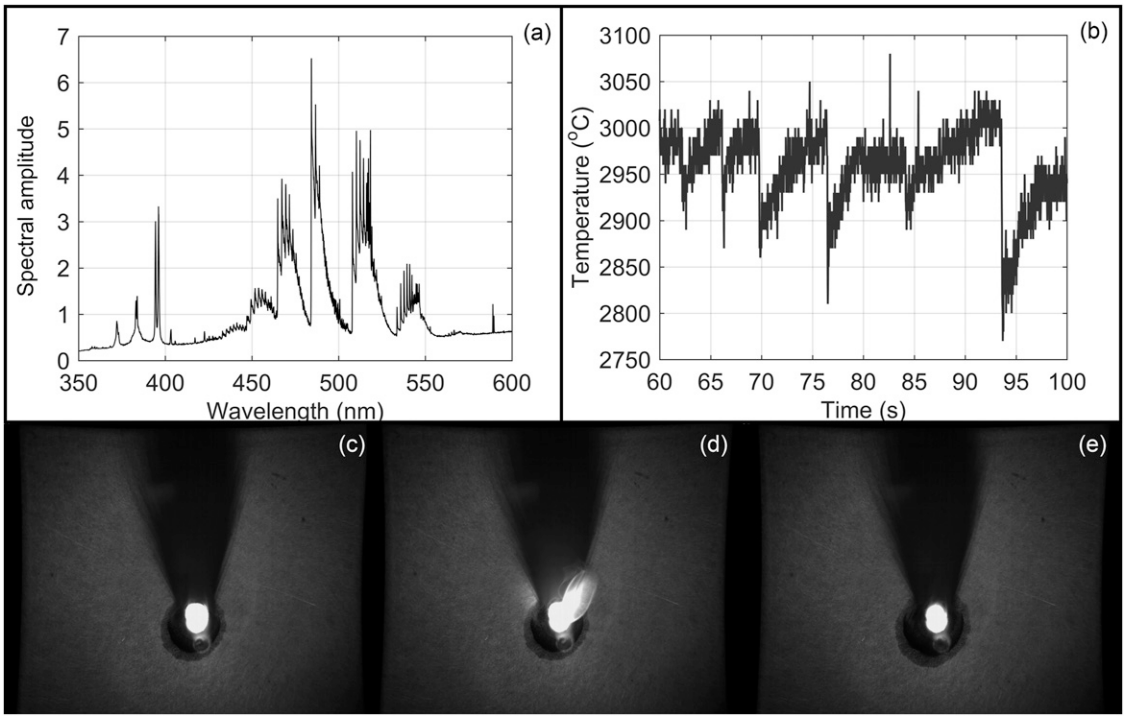

Figure 7. (a) Spectrum measured during the interaction of a HEL with an aluminum coupon. (b) Surface temperature temporal evolution obtained from spectral measurements. (c–e) Still images from the active imager captured at 90 s, 92 s, and 95 s, respectively.

measurement located between 60 s and 100 s after laser initiation to highlight specific aspects. As opposed to the carbon steel samples discussed above, aluminum coupons appear to evaporate at temperatures exceeding 2950 °C, approximately 150 °C above the evaporation temperature for steel. Pure aluminum evaporates at a temperature of 2470 °C, significantly lower than what is shown in the measurement. The discrepancy stems from surface oxidation that is catalyzed under the effect of elevated temperatures. The generated aluminum oxide layer shields the sample's surface and absorbs the laser power. Interestingly, aluminum oxides are known to evaporate at 2970 °C, exactly within the range of measurement shown in Fig. 7b highlighting the accuracy of the method.

From Fig. 7b, each event where the surface temperature appears to exceed the oxide's evaporation temperature is followed by an immediate and drastic temperature drop. This indicates that hot material was evacuated in the plume, revealing a cooler surface waiting to be thermalized by the laser. This is supported by Figs. 7c–7e presenting still images from the active imager, captured, respectively, at times 90 s, 92 s, and 95 s. As shown, the evaporation plume is only visible prior to the reduction of the surface temperature measured with the spectrometer.

It is important to note that variations in the emissivity of the samples exposed to the lasers have not been accounted for in the temperature evaluation. Emissivity is known to vary with temperatures, especially during phase transitions. For single-wavelength (or single band) sensors that evaluate temperatures based on the signal intensity produced by a heated body, emissivity variations can lead to significant errors. However, the spectroscopic signature analysis proposed here is immune to such variations as changes in emissivity do not impact on the spectral distribution; they affect the amount of energy that is radiated.

Emissivity also varies with the emission wavelength, usually decreasing with increasing wavelength for metallic samples. This phenomenon could possibly have affected the measurements presented. In fact, emissivity variations across a spectrum will alter the radiative distribution, effectively producing errors on the temperature measurements. However, significant emissivity variations are reported occurring over spectral ranges spanning from the ultraviolet to the far infrared. In the present work, errors were mitigated by operating a spectroscopic sensor covering a small spectral region in the visible, thus limiting the impact of emissivity variations. This assertion is further supported with the fact that the method was able to identify both the evaporation temperatures for iron (Fig. 5) and aluminum oxides (Fig. 7).

Conclusion

Standoff applications of high-energy lasers present unique challenges. The development of HEL-compatible sensors capable of characterizing the phenomenology from a standoff distance is required for both performance evaluation as well as closed-loop optimization. HELIOS was demonstrated as an efficient spectroscopic technique to discriminate different metallic samples from a long distance.[18]

Here, the method was further tested with a series of systematic experiments conducted in a laboratory setting. The aim was to determine if the technique can be leveraged to assess on the interaction phenomenology in real time. The experiments demonstrated that spectroscopic information available within the signatures can be leveraged to identify optimal interaction regimes. The laser interaction performance with carbon steel coupons was quantified by measuring the time required for the sample's back surface to reach 660 °C; shorter dwell times performing better. Using this metric, interaction regimes where the laser beam maximized material evaporation optimized the reaction and rapidly heated the back surface. For carbon steel, evaporation is always accompanied with iron oxide signatures. Atomic Fe(I) emissions are observed only during acute evaporation events.

This conclusion was further corroborated with spectral temperature monitoring, a powerful feature added to HELIOS capability, which allows standoff quantification of the sample's surface temperature at the interaction point. During evaporation ablation regimes, temperatures saturated at 2800 °C for carbon steel and 2950 °C for aluminum coupons, respectively, coinciding with the evaporation temperatures for iron and aluminum oxide. The information allows identification of laser interaction events such as the material liquefaction (Figure 3) and evaporation (Figs. 5 and 7).

The technique provides real-time insights of the interaction phenomenology without visual observation, enabling standoff assessment of the interaction and, eventually, real-time optimization of the laser beam properties in a closed-loop operation.

Acknowledgments

The authors acknowledge technical support from Pascal Duchesne and Nancy Bérubé.

Declaration of Conflicting Interests

The author(s) declared no potential conflicts of interest with respect to the research, authorship, and/or publication of this article.

Funding

The author(s) disclosed receipt of the following financial support for the research, authorship, and/or publication of this article: This work was supported by the DRDC research project.

Data Availability

Data underlying the results presented in this paper are not publicly available at this time but may be obtained from the authors upon reasonable request.

ORCID iD

Jean-François Daigle https://orcid.org/0000-0003-0180-0969

References

1. A.K. Dubey, V. Yadava. "Laser Beam Machining: A Review". Int. J. Mach. Tools Manuf. 2008. 48(6): 609-628.
2. A. Sharma, V. Yadava. "Experimental Analysis of Nd-YAG Laser Cutting of Sheet Materials: A Review". Opt. Laser Technol. 2018. 98: 264-280.
3. K.-M. Hong, C.S. Yung. "Prospects of Laser Welding Technology in the Automotive Industry: A Review". J. Mater. Process. Technol. 2017. 245: 46-69.
4. M. Foster, R. Beaulieu, L. Blais, G. Caron, et al. "Experimental Investigation on Stainless Steel Welding with a 15 kW Fibre Laser". Can. J. Phys. 2014. 92(3): 246-252.
5. E. Kennedy, G. Byrne, D.N. Collins. "A Review of the Use of High-Power Diode Lasers in Surface Hardening". J. Mater. Process. Technol. 2004. 155: 1855-1860.
6. C. Panwisawas, B. Perumal, R.M. Ward, N. Turner, et al. "Keyhole Formation and Thermal Fluid Flow-Induced Porosity during Laser Fusion Welding in Titanium Alloys: Experimental and Modelling". Acta Mater. 2017. 126: 251-263.
7. L. Wang, M. Mohammadpour, B. Yang, X. Gao, et al. "Monitoring of Keyhole Entrance and Molten Pool with Quality Analysis During Adjustable Ring Mode Laser Welding". Appl. Opt. 2020. 59(6): 1576-1584.
8. S. Shevchik, T. Le-Quang, B. Meylan, F.V. Farahani, et al. "Supervised Deep Learning for Real-Time Quality Monitoring of Laser Welding with X-ray Radiographic Guidance". Sci. Rep. 2020. 10(1): 1-12.
9. F. Bardin, A. Cobo, J.M. Lopez-Higuera, O. Collin, et al. "Closed-Loop Power and Focus Control of Laser Welding for Full-Penetration Monitoring". Appl. Opt. 2005. 44(1): 13-21.
10. V.N. Lednev, P.A. Sdvizhenskii, M.Y. Grishin, A.Y. Stavertiy, et al. "In Situ Laser-Induced Breakdown Spectroscopy Measurements During Laser Welding of Superalloy". Appl. Opt. 2021. 60(5): 1144-1149.
11. C. Liu, L. Xu. "Laser Absorption Spectroscopy for Combustion Diagnosis in Reactive Flows: A Review". Appl. Spectrosc. Rev. 2019. 54(1): 1-44.
12. S. Legnaioli, B. Campanella, F. Poggialini, S. Pagnotta, et al. "Industrial Applications of Laser-Induced Breakdown Spectroscopy: A Review". Anal. Methods. 2020. 12(8): 1014-1029.
13. R.C. Wiens, S. Maurice, F.R. Perez. "The SuperCam Remote Sensing Instrument Suite for the Mars 2020 Rover Mission: A Preview". Spectroscopy. 2017. 32(5): 50–55. https://www.spectroscopyonline.com/view/supercam-remote-sensing-instrument-suite-mars-2020-rover-preview [accessed Aug 22 2022].
14. A. Fleck, J.R. Morris, M.D. Feit. "Time-Dependent Propagation of High Energy Laser Beams Through the Atmosphere". Appl. Phys. 1976. 10(2): 129-160.
15. J. Osterholz, M. Lueck, B. Lexow, M. Wickert. "Neutralization of Improvised Explosive Devices by High-Power Lasers: Research Results from the FP7 Project ENCOUNTER". Proc. SPIE 9990. High-Power Lasers 2016: Technology and Systems. 2016. 99900I. 10.1117/12.2241083
16. Z. Xu, C.B. Reed, R. Parker, R. Graves. "Laser Spallation of Rocks for Oil Well Drilling". J. Laser Appl 2004. 1: 1803. 10.2351/1.5060237
17. D.Y. You, X.D. Gao, S. Katayama. "Review of Laser Welding Monitoring". Sci. Technol. Weld. Join 2014. 19(3): 181-201.
18. J.-F. Daigle, D. Pudo, F. Théberge. "Standoff High Energy Laser Induced Oxidation Spectroscopy (HELIOS)". J. Appl. Phys. 2017. 122(17): 173102.
19. D.M. Paardekooper, C. Holbrook, A.L.L. Vosteen, D. Meuken, et al. "Spectroscopy as Diagnostic Tool to Investigate the HEL–Material Interaction". Technologies for Optical Countermeasures XVIII and High-Power Lasers: Technology and Systems, Platforms, Effects V. Proc. SPIE. 2021. 11867: 123-129. 10.1117/12.2599778
20. J.-F. Daigle, D. Pudo, F. Théberge, J. Fortin. "Spectroscopic Monitoring of FeO Fluorescence for Laser Treatment of Steel Surfaces in Air". J. Laser Appl. 2015. 27(3): 032005.
21. R.W.B. Pearse, A.G. Gaydon. The Identification of Molecular Spectra. London: Chapman and Hall, 1976. P. 297.
22. F. Théberge, M. Auclair, J.-F. Daigle, D. Pudo. "Damage Thresholds of Silicon-Based Cameras for In-Band and Out-of-Band Laser Expositions". Appl. Opt. 2022. 61(10): 2473-2482.
23. J. Powell, D. Petring, R.V. Kumar, S.O. Al-Mashikhi, et al. "Laser–Oxygen Cutting of Mild Steel: The Thermodynamics of the Oxidation Reaction". J. Phys. D: Appl. Phys. 2008. 42(1): 015504. 10.1088/0022-3727/42/1/015504